

Research Paper

Experimental synthesis of ThSiO₄ by fluid-induced alteration of chevkinite-(Ce): Evidence for element mobility and variable crystal structure

M. Stachowicz^{a,*}, B. Bagiński^a, D.E. Harlov^{b,c,d}, P. Jokubauskas^a, W. Matyszczyk^a, J. Kotowski^a, R. Macdonald^{a,e}

^a Department of Geochemistry, Mineralogy and Petrology, Faculty of Geology, University of Warsaw, 02-089 Warszawa, Poland

^b Section 3.6, Deutsche GeoForschungsZentrum GFZ, Telegrafenberg, 14473 Potsdam, Germany

^c Department of Earth Resources, China University of Geosciences, Wuhan 430074, China

^d Department of Geology, University of Johannesburg, P.O. Box 524, Auckland Park 2006, South Africa

^e Environment Centre, Lancaster University, Lancaster LA1 4YQ, UK

ARTICLE INFO

Editor: Dr. Claudia Romano

Keywords:

Thorite
Huttonite
Chevkinite
REE
Th mobility
Dissolution reprecipitation
EBSD
Experimental petrology

ABSTRACT

During a series of high P-T experiments aimed at understanding the hydrothermal alteration of the REE,Ti silicate chevkinite-(Ce), three ThSiO₄ phases (thorite, huttonite, and an amorphous ThSiO₄ variety) were formed, showing a wide range of textures from small discrete grains to large-scale replacement of the chevkinite-(Ce). All three phases have compositions close to ThSiO₄, except that the amorphous type contains small amounts of LREE (≤ 0.025 apfu) and inferred H₂O. The three different forms have been confirmed by electron backscatter diffraction, which has also provided information on the microstructure of the crystals. The earliest phase to form was huttonite, composed of many randomly oriented microcrystals. This was later replaced by thorite via fluid-aided coupled dissolution-reprecipitation. The amorphous type formed both by apparent hydrous alteration of the original crystalline thorite and huttonite. The inferred sequence of events is compatible with thermodynamic constraints on the relative stability of thorite and huttonite.

1. Introduction

As polymorphs, tetragonal thorite [ThSiO₄] can only be distinguished from monoclinic huttonite [ThSiO₄] using x-ray or electron diffraction, or Raman techniques, which commonly is difficult due to the fine grain size of either phase. Furthermore, the crystals are often metamict, making it difficult to identify the precursor crystalline phase (Lumpkin and Chakoumakos, 1988; Seydoux-Guillaume et al., 2007). Harlov et al. (2007) demonstrated that the experimentally determined stability fields for thorite and huttonite were not consistent with those inferred from natural occurrences of these phases or from the previous experimental data of Seydoux and Montel (1997). In a series of hydrothermal experiments involving a natural Th-free monazite with thorium nitrate and silica from 300 to 900 °C at 200 to 1000 MPa, Harlov et al. (2007) found that the ThSiO₄ phase replacing monoclinic monazite took the form of monoclinic huttonite implying that huttonite, associated with isostructural monazite, could exist metastably over a much greater

P-T range than previously thought. Mazeina et al. (2005) noted that both polymorphs of ThSiO₄ are metastable at room temperature but stabilize at higher temperatures relative to their binary oxides. Calorimetric studies of the enthalpies of formation of both thorite and huttonite indicated that the measured enthalpy of the thorite-huttonite phase transition is 6.7 ± 2.5 kJ/mol at 298 K and 1 bar (Mazeina et al., 2005), implying thorite to be the stable phase at low pressures and temperatures.

In a set of experiments at 500 to 600 °C and 200 to 400 MPa, which were aimed at documenting the hydrothermal alteration of chevkinite [(REE,Ca)₄Fe²⁺(Fe²⁺,Fe³⁺,Ti)₂Ti₂(Si₂O₇)₂O₈] to other phases (Bagiński et al., 2024), three ThSiO₄ phases (huttonite, thorite, amorphous ThSiO₄) were formed in nine of the experiments. The source of the Th was the chevkinite. Utilizing electron back scattered diffraction (EBSD) and electron probe micro-analytical (EPMA) analysis of the petrological and mineralogical features of these three ThSiO₄ phases, this study investigates (i) how Th was released from the chevkinite-(Ce) and

* Corresponding author.

E-mail address: marcin.stachowicz@uw.edu.pl (M. Stachowicz).

<https://doi.org/10.1016/j.chemgeo.2024.122429>

Received 21 April 2024; Received in revised form 16 August 2024; Accepted 24 September 2024

Available online 30 September 2024

0009-2541/© 2024 The Authors. Published by Elsevier B.V. This is an open access article under the CC BY license (<http://creativecommons.org/licenses/by/4.0/>).

Table 1

Summary of hydrothermal experiment parameters: temperature (T), pressure (P), duration (Time), initial components, and product composition including ThSiO₄ phase sizes.

Experiment	T (°C)	P (MPa)	Time (days)	Components	Products	Size of ThSiO ₄ phase (µm)
CF-1	600	400	21	Cvk, Ab, Qz, Ca(OH) _{2(aq)} , H ₂ O	Bri, Ttn, Wo, Px*, ESM, Am	rare, up to 40
CF-5	600	200	26	Cvk, Ab, Qz, Byt, Py, Cal, Ca(OH) _{2(aq)} , H ₂ O	Bri, Ttn, Wo, Ab	v. rare, up to 5
CF-6	600	200	26	Cvk, Ab, Qz, Byt, Fap, Py, Cal, Ca(OH) _{2(aq)} , H ₂ O	Bri, Ttn, Wo, Ab, Q	v. rare, up to 30
CF-14	550	200	84	Cvk, Ab, Qz, Ca(OH) _{2(aq)} , H ₂ O	Bri, Ttn, Wo, Px*, Ab, Q	ab., up to 300
CF-15	550	200	84	Cvk, Ab, Qz, Ap, NaF _(aq) , H ₂ O	Bri, Ttn, Mnz, Tkt, Nar, Ap, Flr, Px*	ab., up to 300
CF-18	600	200	42	Cvk, Ab, Qz, Al ₂ O ₃ , Ca(OH) _{2(aq)} , H ₂ O	Bri, Ttn, Pl, ESM, Wo,	up to 100
CF-19	600	200	42	Cvk, An(glass), Qz, Al ₂ O ₃ , Ca(OH) _{2(aq)} , H ₂ O	Pl, Bri, Ttn, Wo, Mnz,	v. rare, up to 40
CF-20	600	200	42	Cvk, Byt, Qz, Al ₂ O ₃ , Ca(OH) _{2(aq)} , H ₂ O	Bri, Ttn, Pl, ESM, Wo	v. rare, up to 20
CF-21	600	200	42	Cvk, Ab, Qz, An (glass), Al ₂ O ₃ , Ca(OH) _{2(aq)} , H ₂ O	Bri, Ttn, ESM, Pl,	v. rare, up to 125
CF-23	600	200	32	Cvk, Qz, An (glass), Kfs, FeO, Mg(OH) _{2(aq)} , Ca(OH) _{2(aq)} , CaF _{2(aq)} , H ₂ O	Bri, Ttn, ESM, Bt, Flr, Fe(OH) ₂	rare, up to 100
CF-24	600	200	32	Cvk, Byt, Qz, Kfs, FeO, Mg(OH) _{2(aq)} , Ca(OH) _{2(aq)} , CaF _{2(aq)} , H ₂ O	Bri, Flr, Pl, Px*, Ttn, ESM, Fe (OH) ₂	up to 200**

Ab – Albite; Ap – Apatite; Bt – Biotite; Bri – Britholite; Cvk – Chevkinite; ESM – Epidote Supergroup Minerals; Fe(OH)₂ – Iron(II) hydroxide; Flr – Fluorite; Nar – Narsarsukite;

Pl – Plagioclase; Px – Pyroxene; Qz – Quartz; Tkt – Turkestanite; Ttn – Titanite; Wo – Wollastonite; aq – Aqueous.

**Note the size of ThSiO₄ in CF-24 with comparison to poor chevkinite reaction; All abbreviations according to Warr (2021); Px* different pyroxenes with different chemical composition.

transported to form these three phases; (ii) the role of fluid chemistry during this process; and (iii) the sequence and conditions under which thorite, huttonite, and the amorphous phase formed.

2. Experimental and analytical procedures

A series of 24 experiments at 550 and 600 °C and 200 MPa have been conducted aimed at understanding the hydrothermal alteration of chevkinite [(REE,Ca)₄Fe²⁺(Fe²⁺,Fe³⁺,Ti)₂Ti₂(Si₂O₇)₂O₈] to other mineral phases and, in particular, the behaviour of the light rare earth elements (LREE) during the alteration. In most of these experiments chevkinite-Ce partly broke down into a series of other phases including fluorbritholite, epidote supergroup minerals; titanite, gagarinite, and fluorite. The experimental technique and results from the 24 experiments are described in detail in Bagiński et al. (2024). In nine of these experiments three ThSiO₄ phases formed, which show an unusual range in textures (Table 1). These included tetragonal thorite (I4₁/amd), monoclinic huttonite, (P2₁/n), and as an amorphous phase.

2.1. High P-T hydrothermal experiments

The starting material for the experiments was a pristine chevkinite-(Ce) from the Diamer district, Pakistan. Omitting elements occurring at levels <0.1 apfu (in CF1 file), the average formula of the starting chevkinite used can be written as: (Ce_{1.85}La_{0.79}Nd_{0.64}Ca_{0.39}Pr_{0.22})_{3.9}Fe²⁺(Fe²⁺_{1.03}Ti_{0.75}Mn_{0.16})_{1.9}Ti₂(Si₂O₇)₂O₈ (Supplementary Table 1). This is close to the standard chevkinite formula A₄Fe²⁺(Fe²⁺Fe³⁺Ti)₂Ti₂(Si₂O₇)₂O₈ (Ito and Arem, 1971). While the major components show relatively little variation, e.g. FeO (all Fe as Fe²⁺) = 10.95–11.98 wt% (average 11.37 wt%), TiO₂ = 16.56–17.11 wt% (average 17.08 wt%) and Ce₂O₃ = 22.35–24.14 wt% (average 23.68 wt%), some minor components are more variable (Supplementary Table 1). The Th content was found to be relatively variable (ThO₂ = 0.54–2.89 wt% (average 0.94 wt%)), which is high for chevkinite but not exceptionally so. In a compilation of 156 chevkinite analyses from the literature, Macdonald et al. (2019) found the Th content to range from below the EPMA detection limit to 4.87 wt% (average 1.15). Detailed EPMA analyses of a chevkinite-(Ce) crystal fragment before the experiments showed that the highest and lowest Th abundances were randomly distributed in the crystal (Supplementary Table 1). EPMA analysis of the residual chevkinite-(Ce) from several experiments, including discrete grains and residual islands, showed that there were no significant compositional modifications during the experiments.

The experiments were undertaken at the Deutsches Geo-ForschungsZentrum Potsdam. The pressure used, 200 MPa, was based on the geological occurrences of alteration of the chevkinite group of minerals, i.e. generally shallow crustal. The temperatures, 550 and 600 °C, are perhaps at the high end of the range for hydrothermal processes but had to be high enough to promote a significant reaction. The experimental duration of the experiments ranged from 21 to 84 days. Natural Amelia albite (Ab₉₉) and quartz were added to the charges to simulate the common host rocks of chevkinite (syenites and granites) more closely. All charges contained 5 to 6 mg H₂O. A range of other components was also added in varying combinations; CaCl₂, CaCO₃, CaF₂, Ca(OH)₂, Ca₃(PO₄)₂, FeS, NaF, fluorapatite, bytownite, anorthite glass, and Al₂O₃ (Table 1). They were chosen to vary such parameters as the alkalinity and H₂O/F ratios of the fluids. The charge + fluid was loaded into a 15 mm long, 3 mm wide Pt capsule, which was then arc-welded shut.

The experiments were carried out using a standard cold seal autoclave in conjunction with a hydrothermal high-pressure line. An internal thermocouple was placed such that its tip was located half-way up along

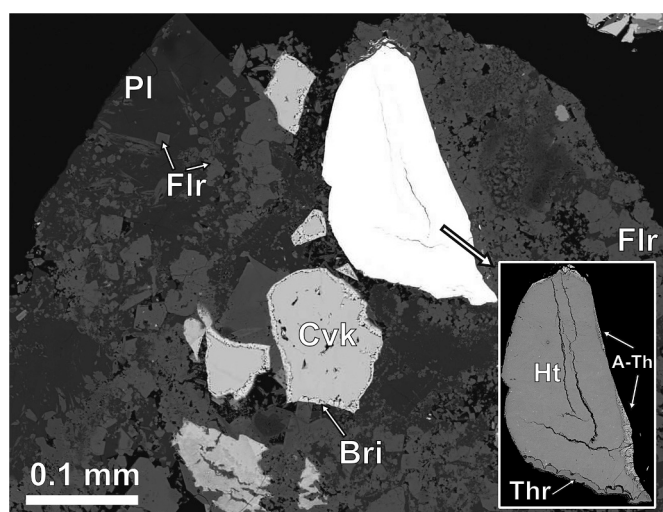


Fig. 1. ThSiO₄ grain consisting of a huttonite core surrounded by thorite and not associated with chevkinite-(Ce) (Cvk). Experiment CF24. Ht – huttonite, Thr – thorite; Bri – britholite; Flr – fluorite; Pl – plagioclase.

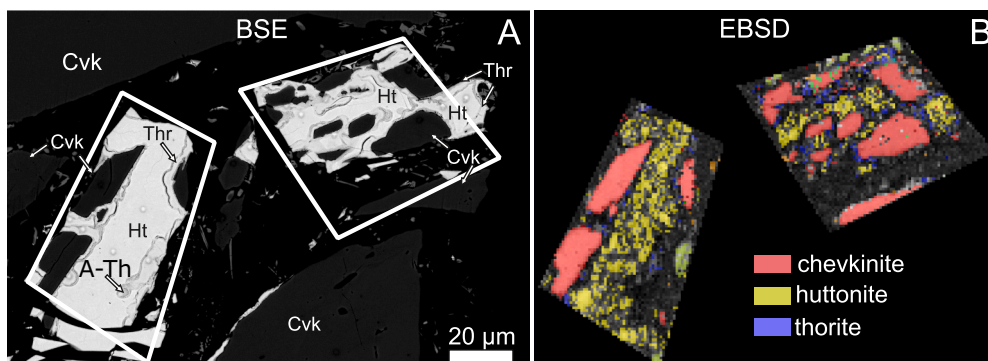


Fig. 2. Chevkinite-(Ce) largely replaced by three ThSiO_4 phases in CF14. (a) BSE image showing huttonite (Ht) to be the dominant Th phase, with thin rims of thorite and amorphous ThSiO_4 . (b) EBSD image of the same grains. Red is chevkinite-(Ce), yellow-green = huttonite, and blue = thorite. (For interpretation of the references to colour in this figure legend, the reader is referred to the web version of this article.)

a sealed platinum capsule placed at the end of the autoclave. The thermocouple is accurate to within ± 3 °C. The maximum thermal gradient along the length of the Pt capsule is ~ 5 °C. Pressure on the hydrothermal line was calibrated against a pressure transducer calibrated against a Heise gauge manometer. After the run, the autoclave was quenched using compressed air. Temperatures of 100 °C were generally reached within 1 min. The charge was then embedded in epoxy and polished. The resulting grain mount was then evaluated using scanning electron microscopy (SEM), EPMA, and electron backscatter diffraction (EBSD) at the Laboratory of Electron Microscopy, Microanalysis and X-Ray Diffraction, Faculty of Geology, University of Warsaw.

2.2. SEM and EPMA

Detailed imaging at high magnifications and preliminary phase identifications were performed using a ZEISS AURIGA 60 FE (field emission) SEM equipped with two Bruker XFlash 6/30 energy dispersive

silicon drift detectors (SDD EDS). Selected crystals were analyzed with a Cameca SXFiveFE electron microprobe, equipped with five wavelength dispersive spectrometers and with large crystals. Samples were cleaned and carbon-coated (20 nm) prior to analysis with a carbon coater (Leica EM ACE200) in pulse mode using a single carbon thread. In this way the carbon coating can withstand an intensive electron beam for an extended analytical time (internal lab samples show a repeatable withstand ability of 200 Na/10 min). All details concerning analytical conditions are available in the Supplementary Tables: raw analyses section). Since a structural analysis is not available for all grains analyzed by EPMA, we refer, for simplicity, to all occurrences as ThSiO_4 unless EBSD data are available.

2.3. Electron backscatter diffraction

EBSD is a technique receiving increasing attention in the Earth Sciences (Prior et al., 2009; Dutta et al., 2022) including isotope analysis (Carr et al., 2017; Taylor et al., 2012; White et al., 2021). EBSD was used to confirm the nature of the ThSiO_4 phases, and to determine the crystallographic orientation within the crystals, which provides information on the growth and replacement mechanisms. The EBSD frames collected are fitted to patterns that are calculated from a data base of crystal structures. The unique diffraction features, known as Kikuchi lines, allow for the differentiation between mineral phases, including polymorphs. Next, their atomic arrangement, orientation with respect to the specimen surface can be identified. Two methods of presenting textures from EBSD information have been utilized here: pole figures and Euler angles (see Section 3.2).

The selected grain mounts were additionally polished using a vibrating polisher for eight hours in a diamond suspension with a grain diameter of $1/4$ μm . Samples were cleaned and carbon-coated (3 nm) prior to analysis with a carbon coater (Leica EM ACE200) in pulse mode using a single carbon thread. EBSD patterns were collected with a Zeiss Auriga electron microscope equipped with a Bruker e – FlashHR+ detector with an integrated ARGUS imaging device. Each sample was tilted to 70° using a dedicated stage (tilt about sample X-axis) for an optimal EBSD signal with the working distance set between 19.2 and 24.7 mm. The detector tilt angle was 2.42° and the sample to detector distance was in the range 15.1 to 16.20 mm. Each experiment was preceded by system calibration, where the sample to detector distance and pattern centre position were determined. The experiments were carried out using an electron beam with an energy in the range 15 to 20 keV. The initial value was 20 keV, which, if needed, was decreased until no drift of the tilted sample was observed. Image tilt correction was used with the Zeiss SmartSEM software and no image rotation was applied. Each EBSD pattern of 400×300 or 800×600 resolution was recorded. The system was calibrated in Bruker ESPRIT 2.1. All the collected patterns were compared to theoretical, simulated Kikuchi lines generated by the Esprit

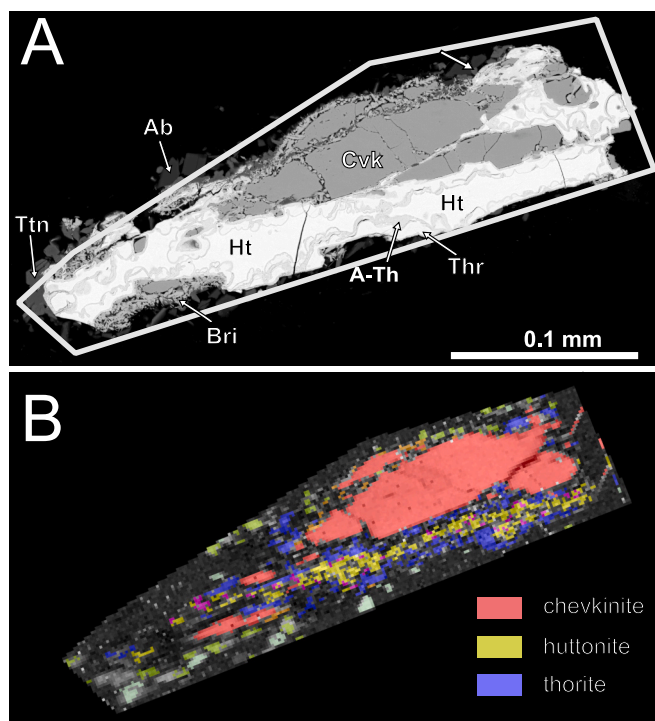
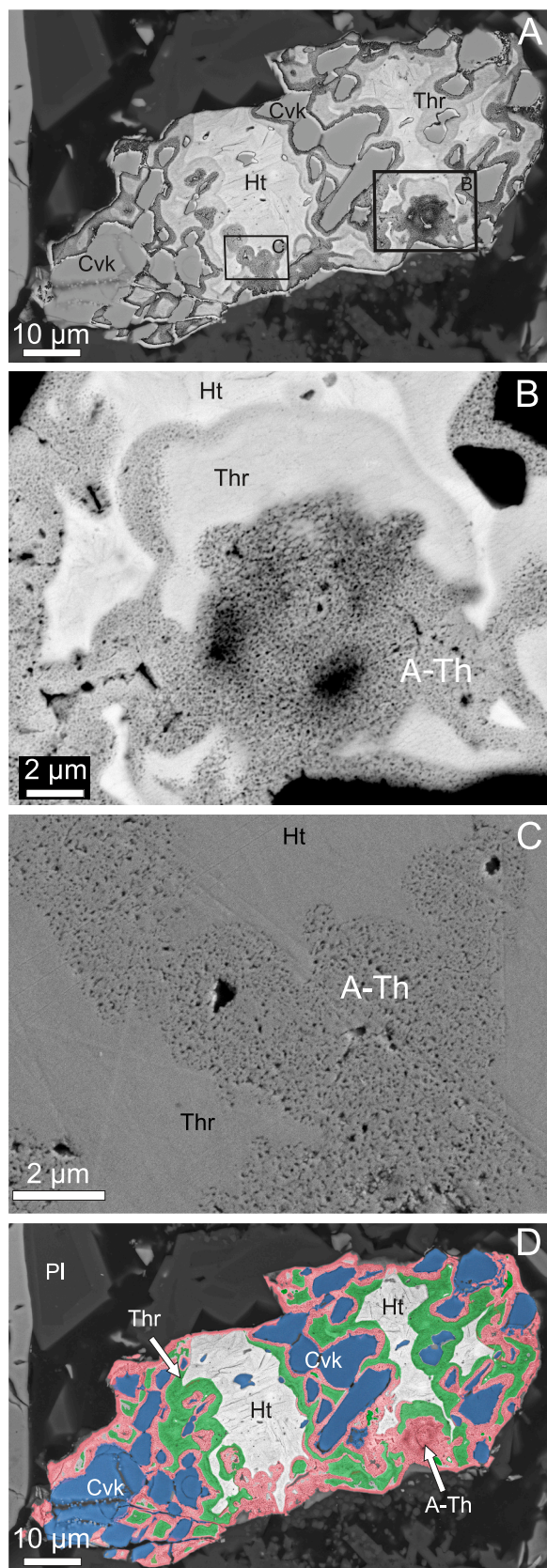


Fig. 3. (a) BSE image of prismatic chevkinite-(Ce) grain, rimmed by britholite (Brh), titanite (Ttn) and minor albite (Ab), and partially replaced by ThSiO_4 phases (CF14). (b) EBSD image of same crystal. Note the close association of thorite and huttonite.



(caption on next column)

Fig. 4. (a) BSE image of chevkinite-(Ce) partially replaced by huttonite (Ht) and thorite (Thr) in experiment CF18. (b) Blow-up of the area in (a) to show complex detail in a spongy zone. Amorphous ThSiO₄ is rimmed by thorite and then by huttonite. (c) In this blow-up of the area in (a) the porosity of spongy area is ~30%. (d) False-colour image of crystal shown in Fig. 4a, providing more detail of the relationships between the Th phases. Chevkinite-(Ce) blue; thorite green; huttonite colourless; amorphous ThSiO₄ red. Note that the ThSiO₄ and thorite form a zone between chevkinite and huttonite. (For interpretation of the references to colour in this figure legend, the reader is referred to the web version of this article.)

2.2 software.

Representative experimental EBSD patterns for huttonite and thorite, together with corresponding simulated patterns, are shown in Supplementary Fig. 1. The crystal structures of huttonite and thorite used to generate simulated patterns for EBSD analysis were taken from Taylor and Ewing (1978).

2.4. First principles calculations utilizing density functional theory

Calculations were run in CASTEP code (Clarke et al., 2005). The cut-off energy and the k-points sampling grid were established based on convergence tests to be 900 eV and 11x11x12 grid, respectively. A PBE functional (Perdew et al., 1996) and geometry optimisation with BFGS minimizer (Pfrommer et al., 1997) were used. The calculations were run at the ACK Cyfronet AGH. We conducted first principles, DFT calculations for both phases at 200 MPa pressure.

3. Textural details

3.1. ThSiO₄ phases

The experimental ThSiO₄ phases show a remarkable range of textures, varying from small, scarce grains (usually ≤20 μm) up to large scale (up to 60%) replacement of the host chevkinite-(Ce) crystal. They also show variable relationships between the three forms of ThSiO₄. In this section, representative examples are described in a sequence depicting the increasing complexity of Th mobility and replacement of the chevkinite-(Ce) and how the different ThSiO₄ phases formed.

In the simplest cases, Th released from the chevkinite-(Ce) was reprecipitated as thorite and/or huttonite separate from the chevkinite-(Ce) grain, where it generally takes the form of anhedral, homogeneous grains from ≤20 μm to 250 μm in size (Fig. 1; CF24).

In contrast, chevkinite-(Ce) can be partly replaced by thorite and huttonite (Figs. 2–4). In Fig. 2a huttonite and thorite are shown replacing chevkinite in experiment CF14. Here the residual chevkinite-(Ce) forms the darker background. EBSD (Fig. 2b) reveals that the dominant ThSiO₄ phase is huttonite (yellow-green), but there are numerous small patches of thorite (blue) as well as some indications of an amorphous ThSiO₄ phase.

Fig. 3a (experiment CF14) shows a prismatic crystal 350 μm long x 60 μm wide where the chevkinite-(Ce), rimmed in places by titanite and britholite, has been partly replaced by huttonite which itself is partly rimmed by thorite with some indications of an amorphous ThSiO₄ phase. Fig. 3b is a phase map from an EBSD experiment superimposed on part of the BSE image in Fig. 3a. The map shows a boundary between the two phases, marked by a thin spongy zone, thorite (blue) on the rim, and huttonite (yellow green) internally. The huttonite consists of a mosaic structure made up of multiple micron to submicron crystals with different orientations. In contrast, the thorite crystals are orientated identically in one crystallographic direction. The huttonite also contains a network of veins of a spongy material, which the EBSD imaging indicates to be amorphous ThSiO₄. The spongy areas show loops and pods following no obvious pattern.

A similar ThSiO₄ reaction texture is shown in Fig. 4, where there has been very extensive replacement of the chevkinite-(Ce) by huttonite,

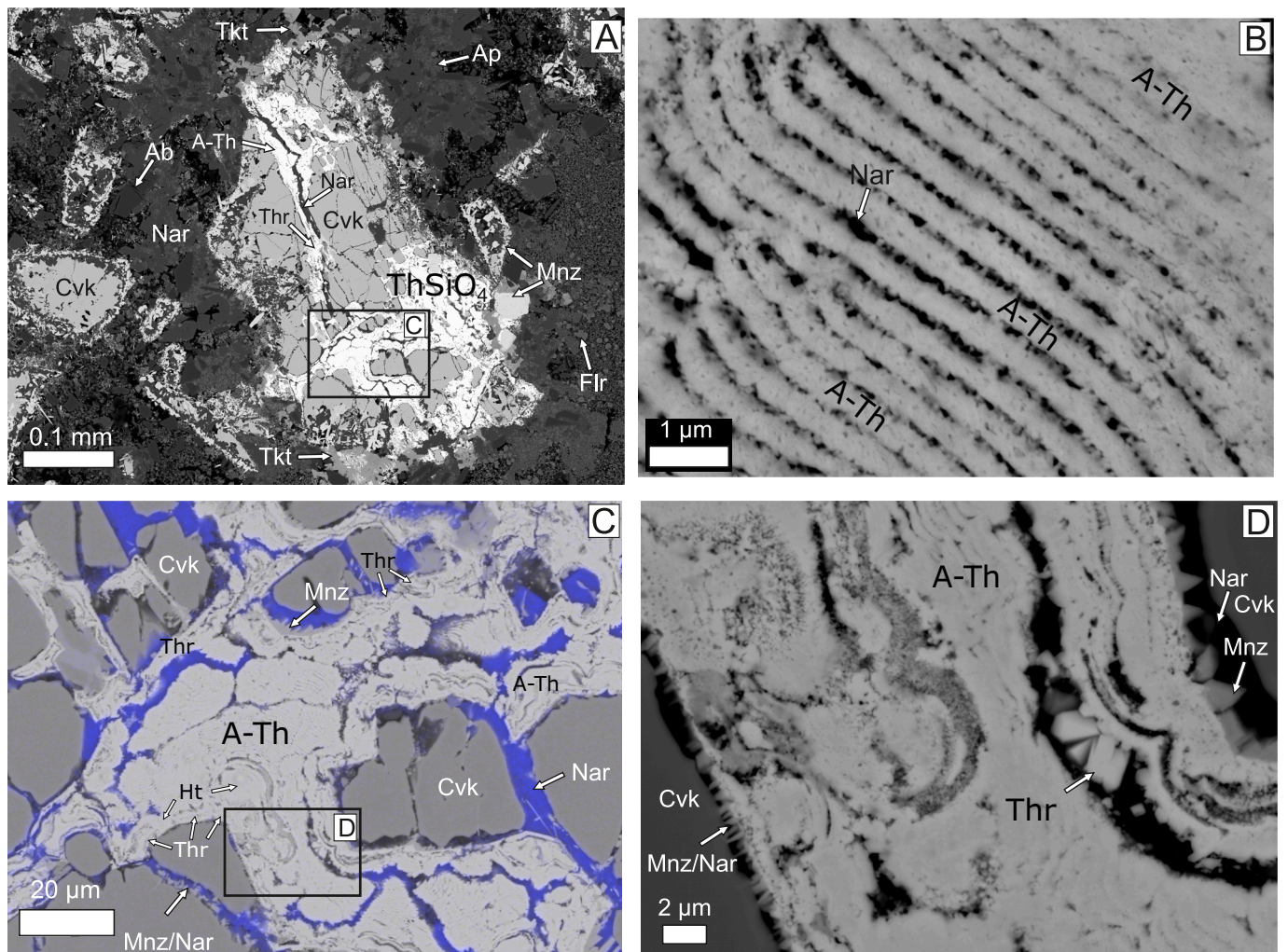


Fig. 5. (a) BSE image of chevkinite-(Ce) (Cvk) partially replaced by veins and patches of amorphous ThSiO_4 from experiment CF15. The internal structure of the veins is complex. Tkt – turkestanite ($\text{Th}(\text{Ca},\text{Na})_2(\text{K}_{1-x}\text{[X]})\text{Si}_8\text{O}_{20}\cdot n(\text{H}_2\text{O})$). (b) Laminar texture with ThSiO_4 layers separated by dark layers containing narsarsukite (Nar). (c) Blocky texture with rims of narsarsukite and monazite (Mnz). Na-rich areas shown in blue. (d) BSE image showing complex structure in small area in (c). (For interpretation of the references to colour in this figure legend, the reader is referred to the web version of this article.)

thorite, and amorphous ThSiO_4 , leaving residual islands of the chevkinite-(Ce). The most likely interpretation is that the reactive fluid initially migrated along cleavages and/or cracks in the chevkinite-(Ce), pervading the interior of the chevkinite-(Ce). The formation of huttonite and subsequent thorite promoted the formation of cracks in the host chevkinite-(Ce). Huttonite, which crystallizes first, has a molar volume of $4.47372 \cdot 10^{-5} \text{ m}^3 \cdot \text{mol}^{-1}$ that is 8 % lower than thorite ($4.8398 \cdot 10^{-5} \text{ m}^3 \cdot \text{mol}^{-1}$) as calculated from their crystal structures (Taylor and Ewing, 1978). This expansion, which accompanies the conversion of huttonite to thorite, expands the cracks in chevkinite, which allow for fluids to penetrate further. The subsequent apparent transformation of thorite to an amorphous ThSiO_4 phase appears to increase the area separating various fragments of the original chevkinite-(Ce) grain from each other (Figs. 4a and 5a). By analogy, macroscopic swelling due amorphization from metamictization can reach up to 16 vol%, for Pu-doped zircon (Weber et al., 1994), or 8 vol%, for externally irradiated LaPO_4 monazites (Picot et al., 2008). Thus, the molar volume of ThSiO_4 is expected to increase with amorphization as the huttonite is isostructural with monazite and thorite with zircon (Seydoux-Guillaume et al., 2012).

The image in Fig. 4a and d shows the relationships between all three forms of ThSiO_4 . Fig. 4b shows detail from a spongy area outlined in Fig. 4a. A dense dark zone is mantled by a grey zone, in turn by a thin darker rim. The spongy amorphous ThSiO_4 area shown in Fig. 4c

dividing the huttonite from the thorite has a 30 % porosity, as measured by digital BSE image processing. A false colour image of the same crystal provides more detail of the relationship between the phases (Fig. 4d). Note that the thorite and amorphous ThSiO_4 form a zone between the chevkinite-(Ce) and huttonite outlining both the chevkinite-(Ce) and the huttonite. There are several spongy amorphous areas (A-Th in Fig. 4) in what appears to have formerly been thorite or huttonite.

The chevkinite-(Ce) in Fig. 5a has been infiltrated, and 35 % replaced, by a series of amorphous ThSiO_4 veins and patches. The veins cut across the grain, frequently changing direction and branching out into patches, especially on the right side. In places, the ThSiO_4 has a mosaic texture (Fig. 5c); elsewhere it has a laminar structure (Fig. 5b), with white ThSiO_4 layers separated by dark layers consisting of narsarsukite [$\text{Na}_2(\text{Ti},\text{Fe}^{3+})\text{Si}_4(\text{O},\text{F})_{11}$]. The laminae are $\leq 1 \mu\text{m}$ wide and number up to 20 across the vein. The replacement has also progressed from the top-left rim along a crack.

Representative compositions of the ThSiO_4 phases are given in Table 2. The full data set is in Supplementary Table 1. Analytical totals for the huttonite are 98.8–100.9 wt%. The only significant replacement for Th is U (4.2–4.7 wt%) along with minor amounts (all <0.5 wt%) of P_2O_5 , Sc_2O_3 , Y_2O_3 , FeO, PbO, La_2O_3 , Ce_2O_3 , and Na_2O . Thorite analyses are very similar to those of huttonite, but with slightly lower contents of U (3.9–4.2 wt% UO_2), Y, La, Ce, Fe, Pb, and Na. Analytical totals

Table 2
Electron probe microanalyses of ThSiO₄ phases.

Number	1	2	3	4	5	6	7	8
Comments	huttonite	thorite	amorphous	thorite	amorphous	huttonite	thorite	huttonite
Sample	CF14-Thr-18	CF14-Thr-26	CF14-Thr-27	CF15-Thr-14	CF15-Thr-16	CF18-Thr-1	CF18-Thr-3	CF24-Thr-10
Constituents ^a	<i>in wt%</i>							
SO ₃	0.05	b.d.	0.06	b.d.	0.05	b.d.	b.d.	b.d.
P ₂ O ₅	0.15	0.04	0.09	0.27	0.30	b.d.	0.08	0.05
SiO ₂	18.99	18.38	18.93	18.56	18.54	18.79	18.64	18.42
TiO ₂	b.d.	b.d.	b.d.	0.16	b.d.	b.d.	b.d.	b.d.
ThO ₂	72.23	75.73	71.36	73.54	73.74	75.56	74.75	75.66
UO ₂	5.10	4.15	3.18	4.51	4.62	4.28	4.15	4.56
Sc ₂ O ₃	0.04	0.04	b.d.	0.04	0.04	0.03	0.05	0.04
Y ₂ O ₃	0.33	0.13	0.35	0.17	b.d.	b.d.	0.13	b.d.
Ce ₂ O ₃	0.49	0.22	0.77	0.58	0.58	0.29	0.31	b.d.
Nd ₂ O ₃	0.46	b.d.	0.53	0.36	0.28	b.d.	0.21	b.d.
Sm ₂ O ₃	0.20	b.d.	b.d.	0.17	b.d.	b.d.	b.d.	b.d.
Gd ₂ O ₃	0.27	b.d.	0.22	b.d.	b.d.	b.d.	b.d.	b.d.
Tb ₂ O ₃	b.d.	b.d.	0.18	b.d.	b.d.	b.d.	b.d.	b.d.
CaO	b.d.	b.d.	0.42	b.d.	b.d.	0.07	0.08	0.05
FeO ¹	b.d.	b.d.	0.12	0.16	b.d.	0.14	0.13	b.d.
PbO	0.11	0.07	b.d.	b.d.	0.09	0.13	0.16	0.1
Na ₂ O	0.33	b.d.	b.d.	b.d.	0.55	b.d.	b.d.	b.d.
K ₂ O	0.03	b.d.	0.07	b.d.	0.03	0.03	0.04	0.06
Total	98.78	98.76	96.28	98.52	98.82	99.32	98.73	98.94
Cations (apfu)	<i>Calculated formulae based on 4 oxygens</i>							
Ti ⁴⁺	0.006							
Th ⁴⁺	0.877	0.938	0.880	0.901	0.900	0.925	0.919	0.936
U ⁴⁺	0.061	0.050	0.038	0.054	0.055	0.051	0.05	0.055
Sc ³⁺	0.002	0.002		0.002	0.002	0.001	0.002	0.002
Y ³⁺	0.009	0.004	0.010	0.005			0.004	
Ce ³⁺	0.010	0.004	0.015	0.011	0.011	0.006	0.006	
Nd ³⁺	0.009		0.010	0.007	0.005		0.004	
Sm ³⁺	0.004			0.003				
Gd ³⁺	0.005		0.004					
Tb ³⁺			0.003					
Ca ²⁺			0.024			0.004	0.005	0.003
Fe ²⁺			0.005	0.007		0.006	0.006	
Pb ²⁺	0.002	0.001			0.001	0.002	0.002	0.001
Na ⁺	0.034				0.057			
K ⁺	0.002		0.005		0.002	0.002	0.003	0.004
Σ	1.015	0.999	0.994	0.996	1.033	0.997	1.001	1.001
S ⁶⁺	0.002		0.002		0.002			0.002
P ⁵⁺	0.007	0.002	0.004	0.012	0.014		0.004	
Si ⁴⁺	1.013	1.001	1.025	0.999	0.995	1.011	1.007	1.001
Σ	1.022	1.003	1.031	1.011	1.011	1.011	1.011	1.003

¹ Total Fe was assumed to be Fe²⁺; b.d. – below detection limit,

* La and Pr were also analyzed, but their content was b.d.

(97.6–99.8 wt%) perhaps indicate the presence of small amounts of OH. Most notably the spongy. Amorphous, form has lower ThO₂ values but much higher LREE (La–Sm). Some analytical totals are low (97.6–99.8 wt%), again perhaps pointing to minor amounts of OH. None of the analyses contains significant amounts of F, even in experiments in which F was added as NaF or CaF₂ (CF15, CF23, CF24).

3.2. Application of EBSD results

In a pole figure, a given direction, (e.g. given unit cell axis direction) is projected on stereographic projection centered on the specimen surface. Thus, pole figures can record whether the orientation of all examined crystals is somehow preferred or random.

In the pole figures the [001] crystallographic axis in chevkinite-(Ce) (Fig. 6d,f) is always projected close to one of four equivalent {111} directions in thorite (Fig. 6e,g, squares of corresponding colours). Fig. 6b,c show where these crystals in their specific orientation are located, with a colouring scheme identical to the one used in pole figures. The phase map (Fig. 6a) distinguishes between chevkinite-(Ce), thorite, and huttonite areas. The method allows us to compare the orientations of neighbouring crystals from various phases. We can see the correlation of the crystal orientation at the contact between the chevkinite-(Ce) and

the thorite.

Euler Angles are a unique set of angles that define the crystal orientation with respect to the specimen surface. They are defined for each analyzed pixel where the EBSD pattern was collected. These angles result from three consecutive rotations necessary to bring crystallographic axes into coincidence with the specimen coordinate system. In a perfect single crystal, all analyzed spots should have identical Euler angles. In reality, mosaic crystals they should fit within a given range, typically 5°. Colouring the specimen by Euler angles bring orientation texture of the analyzed material, *i.a.* indicating sizes of particular crystals.

Fig. 7 shows the Euler angles from the EBSD experiment (Fig. 7a,d) together with the identification of phases (Fig. 7b,e) in the corresponding area. Thorite consists of two fragments with different orientations (blue and orange in Fig. 7a). In contrast, huttonite consists of many small crystals with a random orientation (Fig. 7d), reflected in the Euler representation as multiple, differently coloured, small areas.

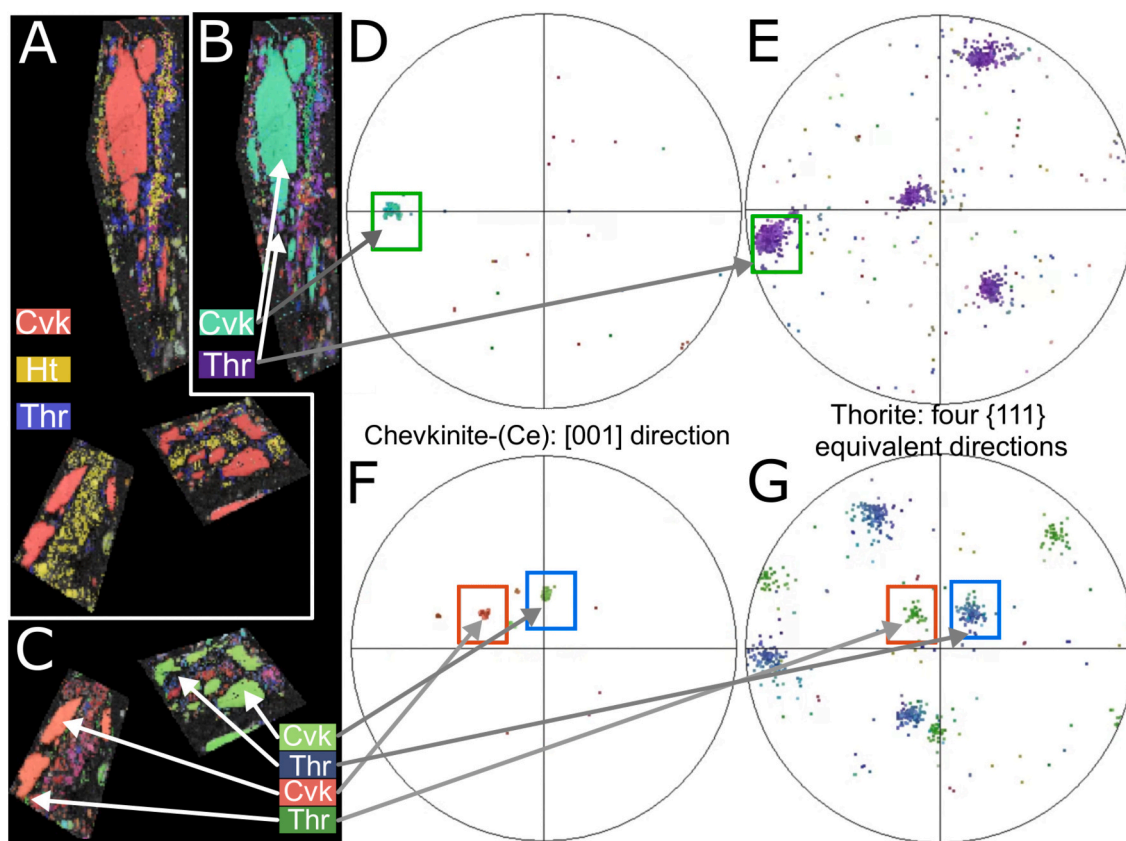


Fig. 6. (a) Phase maps retrieved from EBSD measurements on three areas. (b, c) The corresponding areas are coloured with respect to the crystallographic orientation of the crystals. (d, f) Pole figures showing the projection of the chevkinite-(Ce) crystallographic direction [001], (e, g) and four equivalent {111} directions in thorite.

4. Discussion

4.1. Mobilization and transport of Th

The breakdown of chevkinite-(Ce) to various replacement assemblages, principally britholite-(Ce) and titanite, was almost certainly aided by a coupled dissolution-precipitation process (Putnis, 2002, 2009). Evidence includes sharp compositional boundaries between the chevkinite-(Ce) and the product britholite-(Ce) and titanite, and the presence of fluid-filled pore spaces and porosity in the altered regions.

The extraordinary mobility shown by Th in these experiments lasting only a few weeks also demands a crucial role for fluids. Thorium released at this stage formed the individual crystalline thorite-huttonite grains away from the chevkinite (Fig. 1). Larger-scale replacement of the chevkinite-(Ce) by huttonite and thorite (e.g. Figs. 3a and 4) required a more efficient release of Th from the chevkinite-(Ce) and a mechanism for concentrating it as ThSiO_4 in the replacement texture.

Ca(OH)_2 was added to eight out of nine experiments in which ThSiO_4 formed with various combinations of other phases (Table 1). The most significant replacements were in experiments CF14 (Ca(OH)_2), CF18 (Ca(OH)_2 and Al_2O_3), and CF15 (NaF and $\text{Ca(PO}_4)_2$). In experiments involving Ca(OH)_2 , it seems likely that Th was mobilized as a hydroxyl complex whereas in the case of the experiment involving NaF it was most likely mobilized as a F complex.

Other experimental studies have provided evidence not only on the P-T- $f\text{O}_2$ conditions under which formation of ThSiO_4 takes place but also on the nature and efficacy of the various fluids involved. Harlov and Hetherington (2010), Harlov et al. (2011), and Budzyń et al. (2011, 2017) observed that secondary Th-rich phases did not form during monazite breakdown except when the fluid contained $\text{Na}_2\text{Si}_2\text{O}_5 + \text{H}_2\text{O}$. The results from the NaF-bearing experiment have confirmed, therefore, earlier studies that the presence of alkalis, specifically Na, and

accompanying high pH (as seen for a Ca(OH)_2 solution), enhances Th solubility (Ermolaeva et al., 2007; Harlov and Hetherington, 2010; Budzyń et al., 2011, 2017).

4.2. Huttonite – thorite stability relationships

Under the P-T conditions of the experiments in Table 1, in Fig. 4, huttonite takes the form of a metastable phase that is being partly replaced by its stable polymorph thorite via what appears to be a fluid-aided coupled dissolution-precipitation reaction (Putnis, 2002, 2009). This is also seen in Fig. 1. First principle DFT calculations for both phases, coupled with experimental data (Seydoux and Montel, 1997), show that thorite is more energetically favoured, having a Gibbs free energy of formation lower than huttonite by 15.1 kJ/mol. Furthermore, empirical indications (Ostwald's rules of stages), revealed from EBSD, also point to huttonite being metastable as these crystals grew earlier. Ostwald's rule of stages state that for many crystallizing systems a metastable form will appear first. Once metastable crystals grow, a separate dissolution-precipitation process takes place to form the next more stable phase (Navrotsky, 2004; Ostwald, 1897; Schmelzer and Abyzov, 2017). Moreover, the so-called Ostwald ripening phenomenon encourages the formation of larger crystals via the dissolution of smaller grains, followed by diffusion and subsequent reprecipitation (Huo et al., 2011). Here, aggregates of nano- and micro-crystals of huttonite, all formed in random crystallographic orientations (Fig. 7d). In contrast, the thorite formed larger crystals from the huttonite crystal aggregates with a stronger crystallinity as evidenced by the stronger EBSD diffraction signals (Fig. 7a). In addition, the thorite shows a preferred orientation with respect to the chevkinite-(Ce) where it is in contact (Fig. 8). Thorite, when present (with one exception), can be found on rims partly replacing the huttonite (cf. Fig. 4d), and which are themselves in contact with the chevkinite-(Ce). The orientation of the

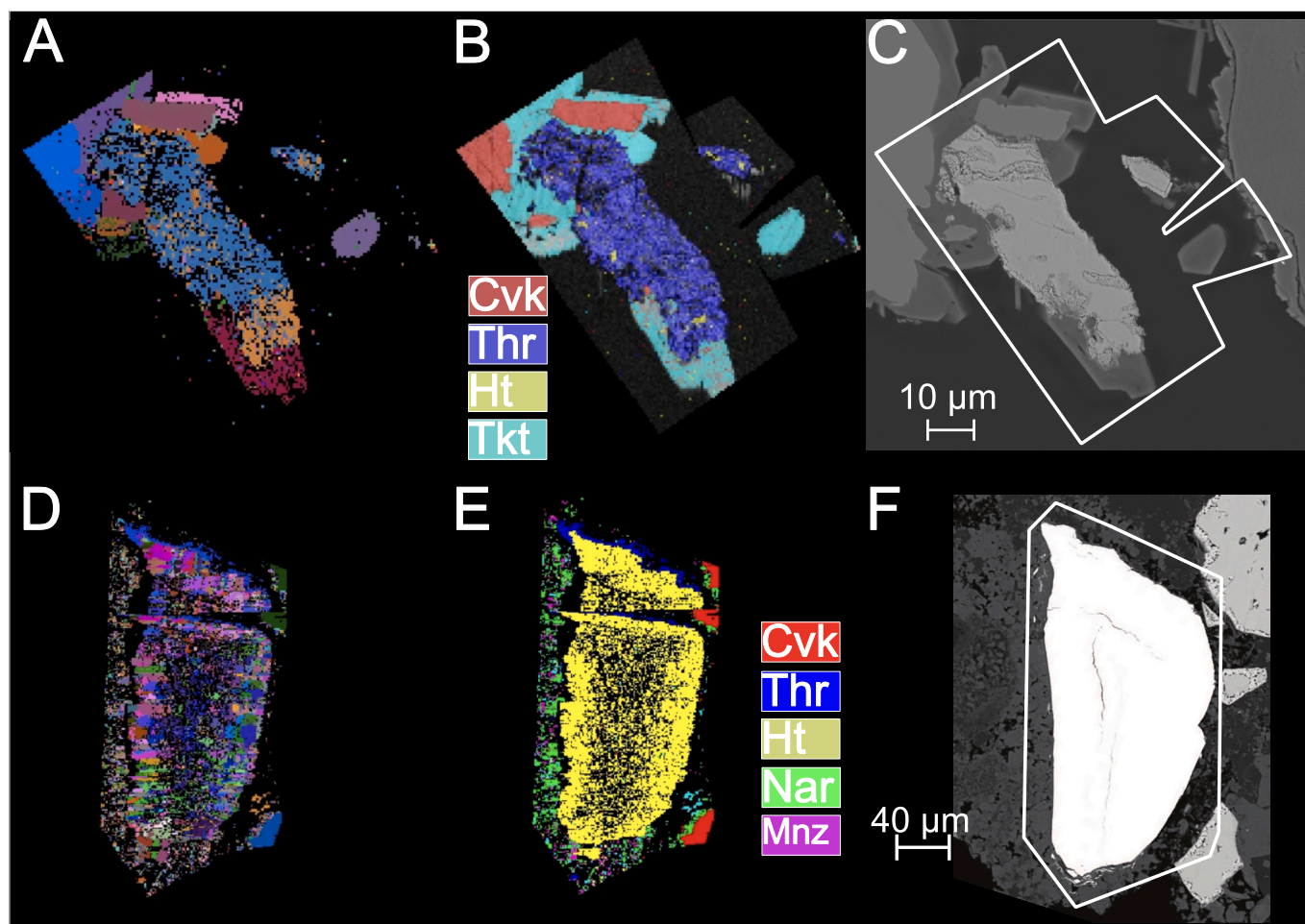


Fig. 7. The Euler angles of crystallites retrieved from EBSD with corresponding phase maps of analyzed areas. (a) Two crystals of thorite (colours blue and orange). (b) Thorite on phase maps is shown as blue, and huttonite yellow. (d) Multiple small crystals of huttonite where various colours indicate different crystallographic orientations. (e) Large block of mostly huttonite in yellow on a phase map with thorite (blue) present on the top as thin layer. (c,f) BSE images of the areas analyzed by EBSD. (For interpretation of the references to colour in this figure legend, the reader is referred to the web version of this article.)

chevkinite-(Ce) crystallographic direction [001] seems to correlate with the [111] direction in thorite. The chevkinite-(Ce) crystals may have acted as a guide or template during formation of the thorite as it replaced the huttonite. Along certain preferred directions REE and Th in these phases show similar arrangement as presented in Fig. 8.

4.3. The amorphous ThSiO_4 zones

The textural evidence is clear that the porous, amorphous ThSiO_4 patches and veins appear to be in the process of replacing crystalline huttonite and thorite (Fig. 4d; Table 2), principally at the contact with chevkinite-(Ce) (Fig. 4d). The amorphous nature of the ThSiO_4 seems to be a response of the thorite or huttonite to hydration. In some of these altered areas, there is a zonal arrangement of amorphous ThSiO_4 – thorite – huttonite (Fig. 4a,b,c), raising the possibility that the thorite was an intermediate phase during the amorphization of huttonite. For example, using petrography coupled with X-ray diffraction of ThSiO_4 grains from the Harding pegmatite, New Mexico, Lumpkin and Chakoumakos (1988) found mixtures of crystalline and amorphous phases, where the amorphous phase was probably due to hydrothermal alteration.

In summary, a combination of the structural data and the textural relationships in Fig. 4 can be used to understand the sequence under which huttonite, thorite, and the amorphous ThSiO_4 formed. This sequence started first with the formation of the huttonite followed by

formation of thorite from the huttonite and later an amorphous ThSiO_4 phase from both the huttonite and the thorite. The formation of this amorphous ThSiO_4 phase most likely was due to the excess H_2O -rich fluids in the capsule, i.e. approximately 14–15 % by mass, during the course of the experiment.

4.4. Application to natural mineral sequences

There is significant empirical evidence from natural sequences on the behaviour of Th during hydrothermal alteration of accessory minerals. During hydrous alteration of two-mica granites from the Massif Central, France, Th remained immobile (Leroy and Turpin, 1988). In a study of monazite breakdown in an orthogneiss from the Western Carpathians, Ondrejka et al. (2012) found that Th released from the monazite did not leave the system in significant amounts. Expansion cracks emanating from fergusonite-(Y) ((Y,REE)NbO₄) in a quartzolite from the Rova occurrence, Keivy massif, are compositionally of two main types, one rich in U (up to 35 wt% UO₂), the other rich in REE (≤ 25 wt% REE₂O₃) (Macdonald et al., 2017a). Abundances of PbO are up to 27 wt%, but ThO₂ levels are much lower (≤ 0.7 wt%). The nature of the vein-filling material and the transporting fluid phase are uncertain but the veins provide evidence of Th mobility during alteration, albeit over short distances, i.e. a few mm. In a study of the formation of ThSiO_4 by hydrothermal alteration of various peralkaline lithologies, Macdonald et al. (2017b) found evidence of short-distance transport of Th on the

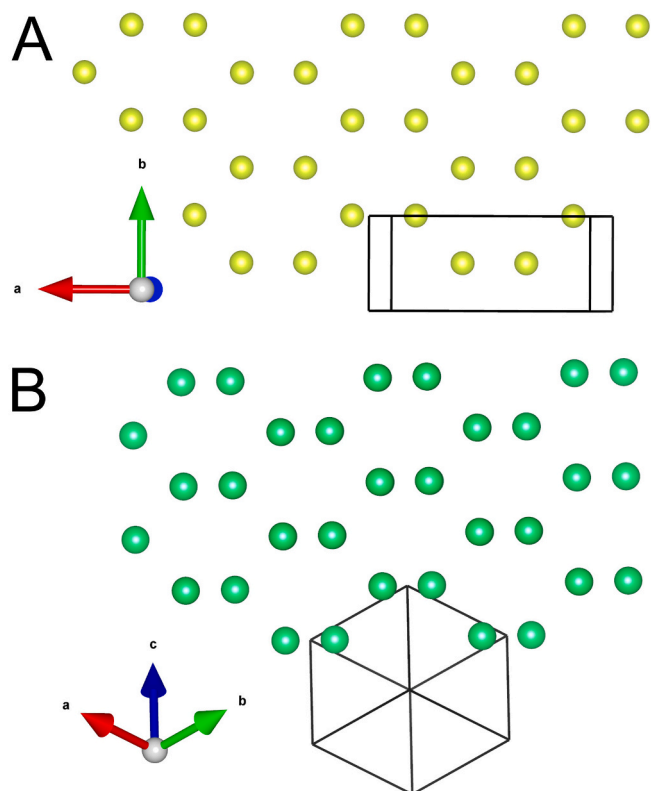


Fig. 8. Similar motifs to show (a) how REE are organized along [001] crystallographic direction in chevkinite-(Ce), and (b) Th atoms in {111} directions in thorite crystal structure.

order of tens to hundreds of microns and suggested that Th was generally retained in the system during alteration, where the system was defined as being no greater than on the hand-specimen scale. Noting that no other Th-rich phases formed during hydrothermal alteration of chevkinite-(Ce) and monazite-(Ce) in the Sin Quyen Fe-Cu-LREE-Au deposit, northwest Vietnam, Li and Zhou (2017) considered Th to have been immobile. They proposed that the fluids were rich in Cl^- and poor in F^- . In a quartz-epidote metasomatite from the Haldzan Buragtag massif, Mongolian Altai, where the hydrothermal fluids were inferred to have been acidic and oxidizing, no secondary Th-rich phases were formed during the breakdown of chevkinite-(Ce) (Macdonald et al., 2015). The evidence, therefore, from both these natural systems and the experimental systems in this study, shows that significant release of Th during the alteration of Th-bearing mineral phases, and its transport in fluids, is generally favoured under alkali-bearing conditions.

Finally, we note that a few studies, e.g., Lumpkin and Chakoumakos (1988), Förster et al. (2000), and Seydoux-Guillaume et al. (2007), have attempted to interpret the structural and compositional factors behind the formation of secondary Th phases during hydrothermal alteration. We contend that the methods used here would be valuable tools in following the various processes and providing further evidence on Th solubility and mobility.

Seydoux-Guillaume et al. (2012) noted that alteration textures in monazite are always associated with radial cracks emanating from radioactive ThSiO_4 causing swelling during metamictization. Cracks, would have helped to facilitate the circulation of fluids, which can then mobilize and carry away dissolved elements (e.g. Fe, Th, Pb, U). The findings presented here show that swelling of ThSiO_4 phases was unrelated to any radiation damage, but rather of a geochemical origin. However, the latter process is of an incomparably shorter duration. It is a balance between a kinetic barrier of transformation and a lowering of the Gibbs free energy. It is also plausible that in the early stage of

crystallization, the configurational entropy favours huttonite over thorite. It is associated with the distribution of other elements such as REE, present in the crystal lattices and can contribute to lowering of the Gibbs free energy. In an alkaline environment, the pronounced presence of ThSiO_4 phases, catalyses the whole process of hydrothermal alteration by the following sequence of events. A rapid transformation process associated with ThSiO_4 swelling cause cracks in the surrounding minerals and further penetration of fluids and subsequent alteration, all in an extremely short period of time.

5. Conclusions and implications

EBSD mapping has proven to be very successful in identifying complex dissolution-reprecipitation steps, specifically here in this study of fluid-aided metasomatic alteration of mineral resulting in a series of phases, including two polymorphs. In this regard, this technique gives us information on phase boundaries similar to that obtained using HR-TEM. Moreover, it is non-destructive for the sample in contrast to the necessity of cutting foils for HR-TEM. Sample preparation is quite simple and similar to standard procedures for SEM imaging. Utilizing this technique, along with EPMA, the following conclusions regarding the results from this study can be made:

- (i) Thorium released during hydrothermal experiments on chevkinite-(Ce) showed significant solubility and mobility in a series of high pH Na- and Ca-bearing fluids in ≤ 84 days, where it may have been transported as hydroxyl complexes, or in the case of NaF, as F complexes.
- (ii) Two Th-bearing polymorph ThSiO_4 phases formed (huttonite and thorite), along with an amorphous ThSiO_4 phase, all in close association with each other.
- (iii) Microtextural relationships indicate that the huttonite formed first but subsequently experienced partial conversion to thorite over the course of the experiment. Empirical considerations and thermodynamic calculations indicate that thorite is the stable phase at 600 °C and 500–550 MPa, whereas huttonite is a metastable phase confirming earlier studies of Seydoux and Montel (1997) and Harlov et al. (2007).
- (iv) The conversion of huttonite to thorite occurred at constant P and T and was the result of kinetic effects related to Ostwald's rules of stages.
- (v) The amorphous ThSiO_4 phase resulted from the direct hydration of the thorite and/or huttonite.
- (vi) The orientation of the chevkinite-(Ce) crystallographic direction [001] appears to have influenced the growth of thorite along the [111] direction.
- (vii) The sequence of ThSiO_4 transformations ultimately leading to amorphization in a very short time scale of ≤ 84 days, indicates an alternative geochemical mechanism in fluid-rich environments as opposed to the widely recognized metamictization resulting from radiation damage.

Supplementary data to this article can be found online at <https://doi.org/10.1016/j.chemgeo.2024.122429>.

CRediT authorship contribution statement

M. Stachowicz: Writing – review & editing, Writing – original draft, Visualization, Methodology, Investigation, Funding acquisition, Conceptualization. **B. Bagiński:** Writing – review & editing, Writing – original draft, Supervision, Funding acquisition, Conceptualization. **D. E. Harlov:** Writing – review & editing, Methodology, Investigation. **P. Jokubauskas:** Methodology, Investigation. **W. Matyszczyk:** Writing – review & editing, Visualization, Methodology, Investigation. **J. Kotowski:** Methodology, Investigation. **R. Macdonald:** Writing – review & editing, Writing – original draft, Supervision, Funding

acquisition, Conceptualization.

Declaration of competing interest

Ray Macdonald reports financial support was provided by National Science Centre Poland. Marcin Stachowicz reports equipment, drugs, or supplies was provided by AGH University of Krakow Academic Computer Centre Cyfronet. If there are other authors, they declare that they have no known competing financial interests or personal relationships that could have appeared to influence the work reported in this paper.

Data availability

Data will be made available on request.

Acknowledgements

We gratefully acknowledge funding by NCN Harmonia grant no. 2017/26/M/ST10/00407.

We acknowledge Poland's high-performance computing infrastructure PLGrid (HPC Centers: ACK Cyfronet AGH) for providing computer facilities and support within computational grant no. PLG/2023/016138.

References

- Bagiński, B., Matyszczyk, W., Jokubauskas, P., Kotowski, J.B., Marciniak-Maliszewska, B., Urbanik, K.M., Harlov, D.E., Stachowicz, M., Macdonald, R., 2024. REE redistribution during the fluid-induced alteration of chevkinite-(Ce): an experimental approach: stability relationships of the REE-bearing phases. Manuscript in preparation.
- Budzyń, B., Harlov, D.E., Williams, M.E., Jercinovic, M.J., 2011. Experimental determination of stability relations between monazite, fluorapatite, allanite, and REE-epidote as a function of pressure, temperature, and fluid composition. *Am. Mineral.* 96, 1547–1567.
- Budzyń, B., Harlov, D.E., Kozub-Budzyń, G.A., Majka, J., 2017. Experimental constraints on the relative stabilities of the two systems monazite-(Ce) – allanite-(Ce) – fluorapatite and xenotime-(Y) – (Y,HREE)-rich epidote – (Y,HREE)-rich fluorapatite, in high Ca and Na-Ca environments under P-T conditions of 200–1000 Mpa and 450–750 °C. *Mineral. Petrol.* 111, 183–217.
- Carr, P.A., Norman, M.D., Bennett, V.C., 2017. Assessment of crystallographic orientation effects on secondary ion mass spectrometry (SIMS) analysis of cassiterite. *Chem. Geol.* 467, 122–133.
- Clarke, S.J., Segall, M.D., Pickard, C.J., Hasnip, P.J., Refson, K., Payne, M.C., 2005. First principles methods using CASTEP. *Zeitschrift für Kristallographie – Crystall. Mat.* 220, 567–570.
- Dutta, D., Maji, V., Abdullah, S., Misra, S., 2022. Application of Electron Backscatter Diffraction (EBSD) Method in Earth Sciences. In: Biswas, K., Sivakumar, S., Gurao, N. (Eds.), *Electron Microscopy in Science and Engineering*. IITK Directions, Springer Nature, Singapore, pp. 61–70.
- Ermolaeva, V.N., Pekov, I.V., Chukanov, N.V., Zadov, A.E., 2007. Thorium mineralization in hyperalkaline pegmatites and hydrothermalites of the Lovozero Pluton, Kola Peninsula. *Geol. Ore Dep.* 49, 758–775.
- Förster, H.-J., Harlov, D.E., Milke, R., 2000. Composition and Th - U - total Pb ages of huttonite and thorite from Gillespie's Beach, South Island, New Zealand. *Can. Mineral.* 38, 675–684.
- Harlov, D.E., Hetherington, C.J., 2010. Partial high-grade alteration of monazite using alkali-bearing fluids: Experiment and nature. *Am. Mineral.* 95, 1105–1108.
- Harlov, D.E., Wirth, R., Hetherington, C.J., 2007. The relative stability of monazite and huttonite at 300–900 °C and 200–1000 MPa: metasomatism and the propagation of metastable mineral phases. *Am. Mineral.* 92, 1652–1664.
- Harlov, D.E., Wirth, R., Hetherington, C.J., 2011. Fluid-mediated partial alteration in monazite: the role of coupled dissolution–reprecipitation in element redistribution and mass transfer. *Contrib Mineral Petrol* 162, 329–348.
- Huo, S.H., Qian, M., Schaffer, G.B., Crossin, E., 2011. Aluminium powder metallurgy. In: *Fundamentals of Aluminium Metallurgy*. Elsevier, pp. 655–701.
- Ito, J., Arem, J.E., 1971. Chevkinite and perrierite: synthesis, crystal growth, and polymorphism. *Am. Mineral.* 56, 307–319.
- Leroy, J.L., Turpin, L., 1988. REE, Th and U behaviour during hydrothermal and superegne processes in a granitic environment. *Chem. Geol.* 68, 239–251.
- Li, X.-C., Zhou, M.-F., 2017. Hydrothermal alteration of monazite-(Ce) and chevkinite-(Ce) from the Sin Quyen Fe-Cu-LREE-Au deposit, northwestern Vietnam. *Am. Mineral.* 102, 1525–1541.
- Lumpkin, G.R., Chakoumakos, B.C., 1988. Chemistry and radiation effects of thorite-group minerals from the Harding pegmatite, Taos County, New Mexico. *Am. Mineral.* 73, 1405–1419.
- Macdonald, R., Bagiński, B., Kartashov, P.M., Zozulya, D., Dzierżanowski, P., 2015. Interaction of rare-metal minerals with hydrothermal fluids: evidence from quartz-epidote metasomatites of the Haldzan Buragtag massif, Mongolian Altai. *Can. Mineral.* 53, 1015–1034.
- Macdonald, R., Bagiński, B., Zozulya, D., 2017a. Differing responses of zircon, chevkinite-(Ce), monazite-(Ce) and fergusonite-(Y) to hydrothermal alteration: evidence from the Keivy alkaline province, Kola Peninsula, Russia. *Mineral. Petrol.* 111, 523–545.
- Macdonald, R., Bagiński, B., Kartashov, P.M., Zozulya, D., 2017b. Behaviour of ThSiO₄ during hydrothermal alteration of rare-metal rich lithologies from peralkaline rocks. *Mineral. Mag.* 81, 872–893.
- Macdonald, R., Bagiński, B., Belkin, H.E., Stachowicz, M., 2019. Composition, paragenesis and alteration of the chevkinite-group of minerals. *Am. Mineral.* 104, 349–367.
- Mazeina, L., Ushakov, S.V., Navrotsky, A., Hoatner, I.A., 2005. Formation enthalpy of ThSiO₄ and enthalpy of the thorite-huttonite transition. *Geochim. Cosmochim. Acta* 69, 4675–4683.
- Navrotsky, A., 2004. Energetic clues to pathways to biomineralization: Precursors, clusters, and nanoparticles. *Proc. Natl. Acad. Sci.* 101, 12096–12101.
- Ondrejka, M., Uher, P., Putiš, M., Broska, I., Bačik, P., Konečný, P., Schmiedt, I., 2012. Two-stage breakdown of monazite by post-magmatic and metamorphic fluids: an example from the Veporic orthogneiss, Western Carpathians, Slovakia. *Lithos* 142–143, 245–255.
- Ostwald, W., 1897. Studien über die Bildung und Umwandlung fester Körper: 1. Abhandlung: Übersättigung und Überkaltung. *Z. Physik. Chem.* 22U, 289–330.
- Perdew, J.P., Burke, K., Ernzerhof, M., 1996. Generalized gradient approximation made simple. *Phys. Rev. Lett.* 77, 3865–3868.
- Pfrommer, B.G., Côté, M., Louie, S.G., Cohen, M.L., 1997. Relaxation of crystals with the Quasi-Newton method. *J. Comput. Phys.* 131, 233–240.
- Picot, V., Deschanel, X., Peugot, S., Glorieux, B., Seydoux-Guillaume, A.M., Wirth, R., 2008. Ion beam radiation effects in monazite. *J. Nucl. Mater.* 381, 290–296.
- Prior, D.J., Mariani, E., Wheeler, J., 2009. EBSD in the Earth Sciences: Applications, common practice, and challenges. In: Schwartz, A.J., Kumar, M., Adams, B.L., Field, D.P. (Eds.), *Electron Backscatter Diffraction in Materials Science*. Springer, US, Boston, MA, pp. 345–360.
- Putnis, A., 2002. Mineral replacement reactions: from macroscopic observations to microscopic mechanisms. *Mineralogical Magazine* 66 (5), 689–708.
- Putnis, A., 2009. Mineral replacement reactions. *Rev. Mineral. Geochem.* 70, 87–124.
- Schmelzer, J.W.P., Abyzov, A.S., 2017. How do Crystals Nucleate and Grow: Ostwald's rule of Stages and beyond. In: Šesták, J., Hubík, P., Mareš, J.J. (Eds.), *Thermal Physics and Thermal Analysis: From Macro to Micro, Highlighting Thermodynamics, Kinetics and Nanomaterials, Hot Topics in Thermal Analysis and Calorimetry*. Springer International Publishing, Cham, pp. 195–211.
- Seydoux, A.-M., Montel, J.-M., 1997. Experimental determination of the thorite-huttonite phase transition. *Terra Nova* 9. Abstract Supplements no. 1. 421.
- Seydoux-Guillaume, A.-M., Wirth, R., Ingrin, J., 2007. Contrasting response of ThSiO₄ and monazite to natural irradiation. *Eur. J. Mineral.* 19, 7–14.
- Seydoux-Guillaume, A.-M., Montel, J.-M., Bingen, B., Bosse, V., De Parseval, P., Paquette, J.-L., Janots, E., Wirth, R., 2012. Low-temperature alteration of monazite: fluid mediated coupled dissolution–precipitation, irradiation damage, and disturbance of the U–Pb and Th–Pb chronometers. *Chem. Geol.* 330–331, 140–158.
- Taylor, M., Ewing, R.C., 1978. The crystal structures of the ThSiO₄ polymorphs: huttonite and thorite. *Acta Crystallogr. Sect. B: Struct. Sci.* 34, 1074–1079.
- Taylor, R., Clark, C., Reddy, S.M., 2012. The effect of grain orientation on secondary ion mass spectrometry (SIMS) analysis of rutile. *Chem. Geol.* 300–301, 81–87.
- Warr, L.N., 2021. IMA–CNMNC approved mineral symbols. *MinMag* 85, 291–320.
- Weber, W.J., Ewing, R.C., Wang, L.-M., 1994. The radiation-induced crystalline-to-amorphous transition in zircon. *J. Mater. Res.* 9, 688–698.
- White, L., Vasconcelos, P.M., Ávila, J.N., Ubide, T., Ireland, T.R., 2021. Crystallographic and crystallochemical controls on oxygen isotope analysis of hematite by SIMS. *Chem. Geol.* 583, 120461.